Variable-rate spray system for unmanned aerial applications using lag compensation algorithm and pulse width modulation spray technology

Zhongkuan Wang,[1,2] Sheng Wen,[1,2] Yubin Lan,[1,2] Yue Liu,[3] Yingying Dong[4]

[1]Guangdong Laboratory for Lingnan Modern Agriculture, College of Engineering, South China Agricultural University, Guangzhou; [2]National Center for International Collaboration Research on Precision Agriculture Aviation Pesticides Spraying Technology, Guangzhou; [3]Anyang Quanfeng Aviation Plant Protection Technology CO., LTD. Anyang; [4]Aerospace Information Research Institute, Chinese Academy of Sciences, Beijing, China

Abstract

To ensure that a variable-rate spray (VRS) system can perform unmanned aerial spray in accordance with a prescription map at different flight speeds, we examine in this paper such significant factors as the response time of the VRS system and the pressure fluctuation of the nozzle during the variable-rate spraying process. The VRS system uses a lag compensation algorithm (LCA) to counteract the droplet deposition position lag caused by the system response delay. In addition, pulse width modulated solenoid valves are used for controlling the flowrates of the nozzles on the variable-rate spray system, and a mathematical model was constructed for the spray rate (L min^{-1}) and the relative proportion of time (duty cycle) each solenoid valve is open. The pressure drop and solenoid valve response time at different duty cycles (50~90%) were measured by indoor experiments. Meanwhile, the lag distance (LD), spray accuracy, and droplet deposition characteristics of the VRS system were tested by conducting outdoor experiments at different flight speeds (4m s^{-1}, 5m s^{-1}, 6m s^{-1}). The results show that LCA can effectively reduce the LD. The LD values of the VRS system with LCA ranged from -0.27 to 0.78m with an average value of 0.32m, while without LCA, the LD values increased to 3.5~4.3m with an average value of 3.87m. The overall spray position accuracy was in the range of 91.56~97.32%. Furthermore, the spray coverage and deposition density, determined using water sensitive paper, were used to evaluate the spray application performance taking into account the spray volume applied. The VRS system can provide the most suitable spray volumes for insecticide and fungicide plant protection products. Based on a prescription map, the optimized VRS system can achieve accurate pesticide spraying as well as desirable spray coverage and deposition density.

Introduction

The application of chemical pesticide, as an essential activity in modern agricultural crop production, improves productivity and product quality. With the commercialization of unmanned aerial vehicle (UAV) technology, agricultural UAVs have become increasingly popular tools in the agricultural field, offering such benefits as terrain adaptation, flexibility, high efficiency, water conservation, and intelligence (Chen *et al.*, 2021). Many advanced technologies, such as GPS navigation, automatic path planning, automatic spraying systems, high precision real-time kinematic (RTK) positioning, and obstacle avoidance technologies, have been adapted for multi-rotor UAVs to improve their operational stability, efficiency, accuracy, and ease of operation (Chen *et al.*, 2021). Having been applied to the protection of wheat (Gómez-Candón *et al.*, 2014), rice (Shi *et al.*, 2021), cotton (Chen *et al.*, 2021), and other crops, the technology of using plant protection UAVs on field crops is becoming increasingly mature.

Currently, most crop protection UAVs typically apply pesticides at a constant rate throughout the field application regardless of the presence or absence of pests, crop density, or canopy characteristics, which results in lower application efficiency (Grella *et al.*, 2022). Recently, Biglia *et al.* (2022) tested a target spray application in vineyard with the main aim to pass from broadcast UAV spray application to canopy-targeted spray applications. This represents the first step: apply pesticides just to the target minimizing ground losses. Variable rate technology (VRT), as one of the key precision agriculture technologies, rationalizes pesticide use (Fabiani *et al.*, 2020). UAV-based VRT pesticide applications have been extensively researched by academics for precise field management of crop

pests and diseases. One implementation of VRT pesticide applications uses position coordinates and a prescription map to alter the pesticide application rate. The spray rate varies as the sprayer passes through the farm (Baio *et al.*, 2018; Mancini *et al.*, 2019). For four crop production (winter wheat, canola, corn, and sugar beet), a 40% to 60% reduction in herbicide dose was achieved through site-specific herbicide applications (Jensen *et al.*, 2012).

In the early 2000s, a number of helicopters began to be equipped with variable rate applicators to meet the site-specific needs of the crops (Jay, 2003; Smith, 2001). In recent years, Huang *et al.*, (2008) proposed a high-precision spraying system applicable to a single-rotor plant protection UAV and achieved precision spray at specific locations. With the development of remote sensing technology, remotely sensed imagery combined with variable-rate aerial applications has been used for site-specific weed management. The VRS system was loaded on an agricultural aircraft and the operating process included weed detection, creation of prescription maps based on remotely sensed imagery, variable-rate system configuration, and site-specific aerial application and evaluation. The operation demonstrated the feasibility and potential for precision aerial spraying in large fields (Yang and Martin, 2017). Hunter *et al.*, (2020) integrated weed identification and sprayers into a multi-rotor UAV integrated system (UAV-IS) and found that the UAV-IS boosted the spraying efficiency by 0.3 to 3 folds compared to ground-based mechanical spraying while minimizing the treatment of non-weeded areas. UAV-IS treated 20% to 60% less of a non-weed area than ground machines, but also missed up to 26% of target weed area, so the accuracy of UAV variable rate spraying applications needed to be further improved.

The UAV-based VRS system has a higher demand on the accuracy and stability of the control system. Many factors can affect the accuracy of pesticide spraying locations, such as GPS output frequency, application response time, spray device response time, flight speed, and so on *(Hunter et al.*, 2020). Compared to ground machinery, UAVs have a faster flight speed and the control system needs faster output control signals (Yang *et al.*, 2018). Thomson *et al.*, (2009) have previously evaluated the response and accuracy of aerial VRS systems when spray rate changes rapidly. The average droplet deposition position error in the moving direction was 5.0m, with a 3.04% error between sprayer rate and prescription rate. To improve the spray position accuracy, researchers have mostly focused on reducing the response time of the VRS system, which is still not effective in eliminating the droplet deposition position errors (Huang *et al.*, 2008; Qi *et al.*, 2021). In particular, when the prescription map decision unit is relatively small, frequent changes in the prescription rate can further reduce the accuracy of the spraying position (Gómez-Candón *et al.*, 2012).

The spray accuracy of VRS systems is largely influenced by the flowrate control technology. The flowrate control system should meet the requirements for spray quality and real-time performance. Pressure-based sprayers that vary the spray volume by changing the pulse width modulation (PWM) voltage of the pump have been widely studied (Zhu *et al.*, 2010). However, since the velocity of the liquid flowing from the nozzle changes, pressure-based systems not only have a slow response but also affect the spray distribution and droplet diameter (Giles and Comino, 1989). Koo (2019) tested the nozzle pressure response characteristics of a UAV variable rate spray system, and found that the nozzle pressure response was delayed by 2.6~3.8s when the pressure-based spray system was turned on/off. Compared to pressure-based spray systems, spray systems controlled by PWM solenoid valves (PWM systems) are a variable rate spray technology that can minimize the application errors caused by pressure changes during operation to

the maximum extent possible (Salcedo *et al.*, 2021; 2022). Each solenoid valve of the PWM system is connected to a nozzle, by controlling the relative time ratio that each solenoid valve stays open, the flowrate can be changed in real-time while maintaining the operating pressure (Butts *et al.*, 2019; Silva *et al.*, 2018). According to Salcedo (2020), a variable-rate sprayer controlled by a laser-guided PWM system reduced spray volume by more than 65 percent when compared to a constant-rate application of the same sprayer. PWM system can still provide sufficient droplet deposition and coverage for an effective insecticide application without over-application. As a result, PWM solenoids have been used in ground-based variable rate sprayers developed for precision spraying so that agricultural chemicals can be applied according to crop requirements. However, the applied research of PWM system in plant protection UAV is still insufficient. The main reasons are as follows: on the one hand, Mangus *et al.*, (2017) discovered through laboratory simulations that the accuracy of spray coverage decreases with decreasing duty cycle due to internal on/off delay of the solenoid valve and alternating on/off interaction of adjacent nozzles. As a result, as the duty cycle decreases, the actual spray uniformity decreases, resulting in under- or over-application. On the other hand, if the pipe length between the solenoid valve and the nozzle is excessive, the frequent on/off of the solenoid valve may cause a water hammer effect. The water hammer effect can cause drastic fluctuations in operating pressure, which can change spray parameters such as spray width and droplet diameter. While, at the same time, the PWM system must also be lightweight due to load and volume limitations. Based on the above considerations, the objectives of this study are: i) to develop a VRS system based on a six-rotor electric UAV to precisely change the spray rate according to the prescription map. A lag compensation algorithm is proposed to reduce the lag distance (LD) of the spray droplets; ii) the control parameters of the PWM system will be experimentally tested in the laboratory to evaluate the pressure drop of the PWM system for different duty cycles. The droplet diameter is also to be evaluated based on the operating pressure at different spray rates; iii) field experiments will be conducted to verify the effectiveness of the spray lag compensation algorithm and to evaluate the field performance and spray quality of the VRS system.

Materials and Methods

Machine set-up

The VRS system (shown in Figure 1) uses RTK technology to obtain position coordinates. RTK is a technique used to increase the accuracy of the Global Navigation Satellite System (GNSS) receiver positions using a fixed base station, that wirelessly sends out correctional data to a moving receiver. In this way, the GNSS receiver can be positioned with sub-centimeter accuracy. The RTK base station is fixed vertically on the ground, while the GNSS receiver (Guangzhou Hi-Target Navigation Tech Co., Ltd. Guangzhou, China) and antenna are placed on top of the UAV. The VRS test platform for aerial pesticide spraying is a six-rotor electric UAV with a recommended spray width of 6m. The UAV has two brushless water pumps that can be turned on/off remotely via remote control. Six PWM solenoid valves (LVM20R2-5A, SMC Corporation, Tokyo, Japan), each weighing 80g, are used to control the flowrate of pesticide spraying. The PWM solenoid valves are installed under each respective rotor. Each solenoid valve was placed closely above the fan nozzle XR110015 VS (TeeJet, Spraying Systems Co., Wheaton, Illinois USA) to avoid the water hammer effect. When the spray rate is 0, the

return solenoid valve installed on the return line opens, allowing the liquid to return to the tank without shutting down the brushless pump. The VRS controller has 2 USB ports and 1 RJ-45 port for connecting external devices, and the on/off button is the master power switch. The operator can observe the operating status of the VRS system on the panel of the controller.

Variable-rate spray control system

The components of the VRS control system are shown in Figure 2. The control system mainly consists of GNSS receiver, controller (Raspberry Pi 4B), lithium battery, duty cycle (DC) converter, DC output transistor amplifier isolation board (TKDM-3A-624-B, Shanhao Automation Co., Ltd, Dongguan, China), return

Figure 1. A six-rotor electric unmanned aerial vehicle with variable-rate spray system.
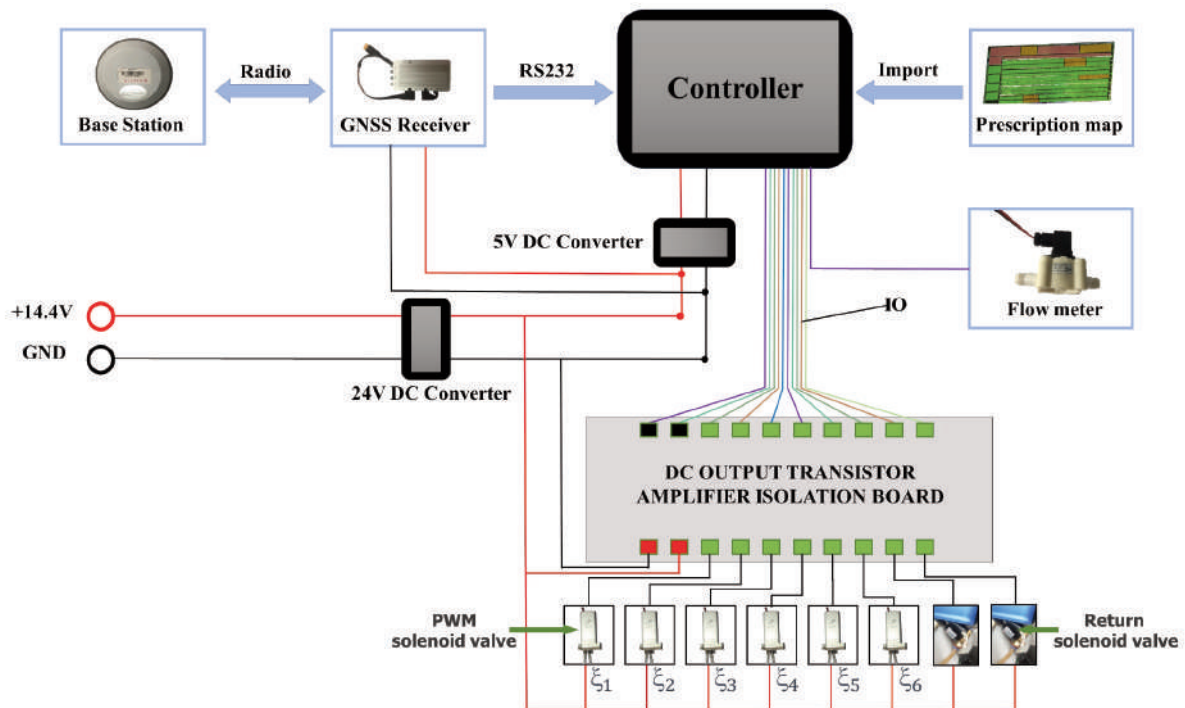

Figure 1. A six-rotor electric unmanned aerial vehicle with variable-rate spray system.

solenoid valve, and PWM solenoid valve. The DC converter converts the 14.4V from the lithium battery to the target voltage to power the GNSS receiver, controller, DC output transistor amplifier isolation board, and solenoid valve, respectively. The GNSS receiver sends the signal to the controller at a frequency of 5Hz via standard RS232 in National Marine Electronics Association 0183 (NEMA 0183) format. After receiving the data, the controller selects and parses the GPRMC string to obtain the longitude, latitude, flight speed, and course angle. The program reads every 0.2s and clears the stacked data to prevent receiving duplicate data. Next, the lag compensation algorithm (LCA) is run to reduce errors in the spray position.

The basic idea of the lag compensation algorithm is as follows: firstly, the position of the UAV in the flight direction is advanced according to the compensation distance to get the compensation coordinates of the UAV. Then a grid search is performed on the prescription map using the compensation position instead of the real position of the UAV to obtain the spray volume (L ha^{-1}). Finally, the control parameter (duty cycle) is calculated from the spray volume and the flight speed. The controller sends control signals to the DC output transistor amplifier isolation board to drive the PWM solenoid. Eventually, the spray rate of the PWM system varies with the duty cycle.

Pulse width modulation system

The design requirements of the sprayer are a faster response rate and a stable droplet diameter. The spraying device consists of a pesticide tank, two brushless pumps, two return solenoid valves, and six PWM solenoid valves. Each brushless pump is rated at 5L min^{-1}. The PWM solenoid valve installed under each rotor operates at a frequency of 11Hz and changes the flowrate by adjusting the proportion of the relative time (duty cycle) that the solenoid valve is open. At 0% duty cycle, the pulse width is 0ms and the valve is completely closed. The PWM solenoid valve is a normally open solenoid valve connected to two fan nozzles recommended for PWM system, and the return solenoid valve is a normally closed solenoid valve. After the program is initialized, the PWM solenoid valve and the return solenoid valve are automatically set to a high level. When the UAV enters the interior of the prescription map, the return solenoid valve is closed while the PWM solenoid valve regulates the flowrate according to the duty cycle. When the prescription rate is zero or the UAV is outside the prescription map, the return solenoid valve opens, allowing the pesticide to flow back into the tank so that the brushless pump does not get clogged or damaged.

After interpreting the prescription map based on the compensation coordinates to obtain the spray volume (L ha^{-1}), it is necessary to convert the spray volume to the prescription rate (L min^{-1}). The calculation is as follows:

$$Q = \frac{60BVP_v}{10000} \tag{1}$$

where Q is the prescription rate (L min^{-1}), B is the spray width (m), V is the flight speed (m s^{-1}), and P_v is the spray volume (L ha^{-1}).

PWM system exhibits larger droplet diameter at lower duty cycles; this is caused by a variety of factors, such as solenoid valve response delays, fluid characteristics, and others. Due to the limitation of duty cycle, the spray rate cannot be further reduced. To achieve a wider range of flow rate variations, nozzles can be controlled individually or in pairs. When the spray rate is low, PWM

solenoids ξ_5, ξ_6 are chosen to close, allowing the spray volume to be reduced while maintaining a high duty cycle. When solenoid valves ξ_5, ξ_6 are closed, the number of nozzles in operation is reduced from 12 to 8. After laboratory experiments were performed to test the spray rates at different number of nozzles and duty cycles, the spray rate as a function of duty cycle was obtained and shown as (Eq. 2). Through observation of the nozzle installation position, it can be seen that the nozzles controlled by PWM solenoid valves ξ_1, ξ_2, ξ_3 ξ_4 are sufficient to ensure the spray coverage. Through experimental tests, it was found that there was little effect on spray uniformity when the nozzles controlled by PWM solenoid valves ξ_5, ξ_6 were turned off. When the prescription rate is changed, the DC for the new spray rate can be calculated from (Eq. 2).

$$DC = \begin{cases} 17.67Q - 9.874; & 4 \le Q \le 6 \quad (12 \text{ nozzle}) \\ 18.73Q + 17.557; & 2 \le Q < 4 \quad (8 \text{ nozzle}) \end{cases} \tag{2}$$

when Q is 4L~6L min^{-1}, every PWM solenoid valve is in the spray state (12 nozzles operating). When Q is 2L~4L min^{-1}, PWM solenoid valves ξ_5 and ξ_6_5 are closed (8 nozzles operating).

Lag compensation algorithm

When the VRS system acquires a new spray rate from the prescription map, the control system cannot adjust the spray rate instantaneously; this can lead to a lag in the droplet deposition position relative to the prescription position. The LCA is therefore proposed to improve the spray position accuracy of VRS control system. Figure 3 shows the idea of LCA. The receiver compensation coordinates are obtained by advancing the compensation distance S in the direction of the UAV flight. After that, the spray rate is obtained from the prescription map using the compensated coordinates instead of the actual coordinates of the receiver. Finally, the duty cycle calculated from (Eq. 2) is used as a control command to adjust the spray rate of the system. Hence, the actual spray rate at the compensation position can be obtained at the exact moment when the UAV reaches the compensation position. The accuracy of the S used to compensate for LDs is key to ensuring accurate pesticide spraying. S is influenced by two factors: the total delay time T of the system and the flight speed V. After performing laboratory experiments to test the factors affecting the total delay time, it was found that T can be divided into the following three parts: the time T_1 associated with the receiver output frequency, set to 0.1s; the program execution time T_2, set to 0.42s; and the time T_3 between the receipt of the control signal by the spraying device and the formation of a stable spraying rate, set to 0.45s. S is calculated as follows:

$$S = V(T_1 + T_2 + T_3) \tag{3}$$

Figure 4 shows the geodesic C of $A(\phi_A, \lambda_A)$ and $B(\phi_B, \lambda_B)$ on an ellipsoid. The steps to calculate the compensation coordinates are shown in Table 1. Point A indicates the current position of the UAV and point B indicates the compensated position of the UAV. The compensation distance (S) is expressed using the length of the geodesic curve C, which defines the shortest curve distance between two points. The angle between the geodetic line and the meridian of the ellipsoid is called the azimuth angle, which in this application indicates the course angle. Here ϕ and λ represent latitude and longitude respectively. The normal of points A and B intersects the axis

of rotation of the ellipsoidal plane at H_A, H_B, and the equatorial plane at angles ϕ_A, ϕ_B. Here α is the length of semi-major axis of the ellipsoid and is the length of semi-minor axis of the ellipsoid. The formula for calculating the geodesic distance and longitude differ-ence between two points on the geodesic line is derived from the solution of the elliptic integral. These integrals do not have direct solutions but are solvable by expanding them into trigonometric series and integrating them term by term (Seong and Choi, 2007).
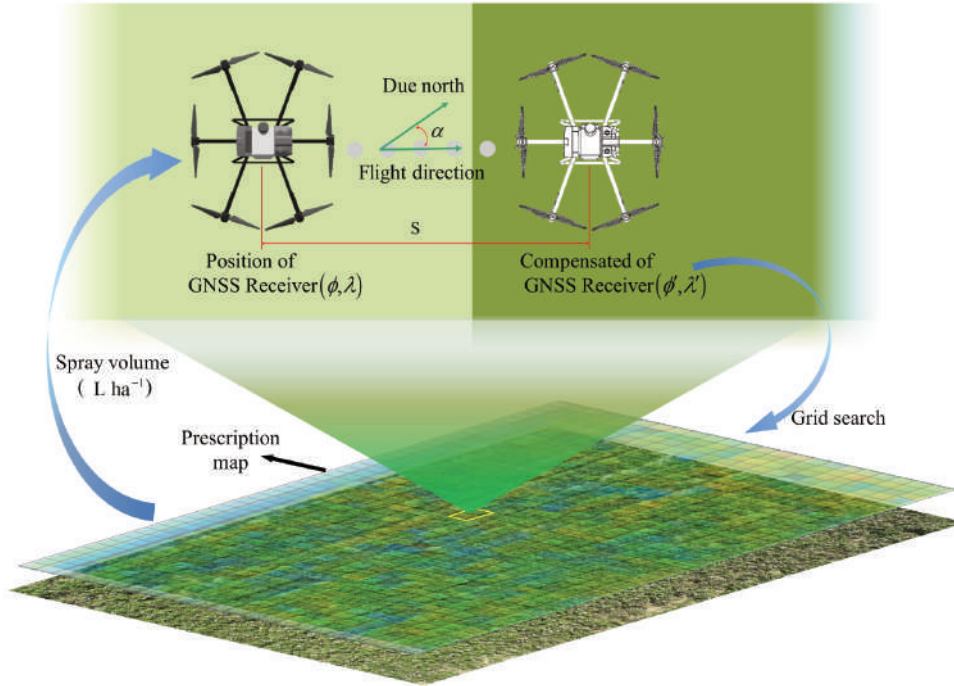

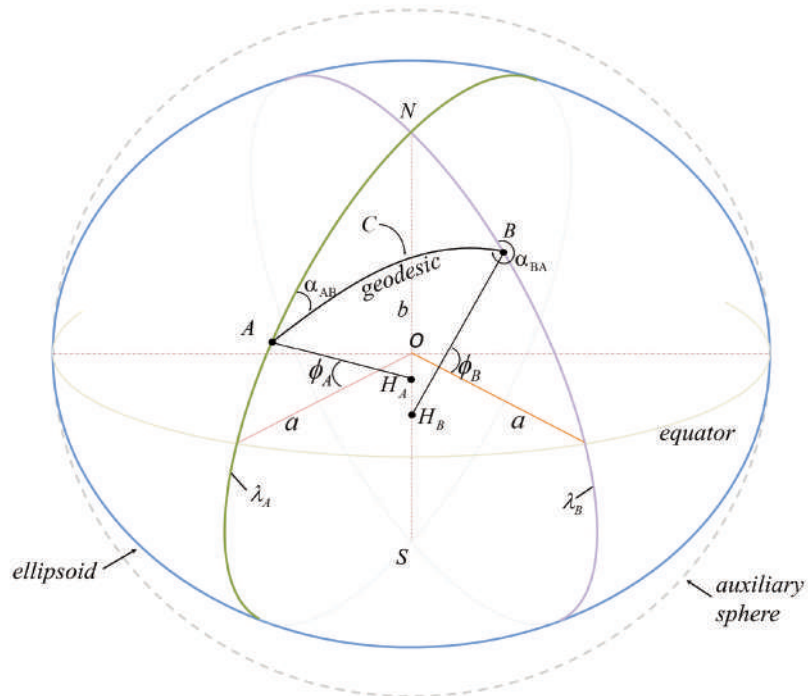**Figure 3.** Schematic diagram of the lag compensation algorithm.

Figure 4. Geodesic on auxiliary sphere.

The solution formulas are as follows:

The reduced latitude U_1 of $A(\phi_A, \lambda_A)$ can be calculated from

$$U_1 = \arctan\left[1 - f \cdot \tan\phi_A\right] \tag{4}$$

where f is the flattening of the ellipsoid, $f=(a-b)/a$. Calculate the angular distance α_1 from the equator to point A on the auxiliary sphere and the forward azimuth of the geodesic at the equator α.

$$\tan\sigma_1 = \tan U_1/\cos\alpha_{AB} \tag{5}$$

$$\sin\alpha = \cos U_1\sin\alpha_{AB} \tag{6}$$

Compute the angular separation α between A and B on the auxiliary sphere using the following equation in iterations until the result is stable. where the first-order approximation in the iterative solution can be taken as $\alpha=S/bJ$.

$$2\sigma_m = 2\sigma_1 + \sigma \tag{7}$$

$$\Delta\sigma = K\sin\sigma\left\{\cos(2\sigma_m) + \frac{1}{4}K\left(\cos\sigma\left[-1 + 2\cos^2(2\sigma m)\right]\right.\right.$$
$$\left.\left. - \frac{K}{6}\cos[2\sigma_m][-3+4\sin^2\sigma][-3+4\cos^2(2\sigma_m)]\right)\right\} \tag{8}$$

$$\sigma = \frac{S}{bJ} + \Delta\sigma \tag{9}$$

As shown below, the calculation formulas of J and K are formulas (10) and (11) respectively. Also, $u^2 = \cos^2\alpha \cdot \left(\frac{a^2-b^2}{b^2}\right)$.

Once α is obtained with sufficient accuracy, spherical triangulation method can be used to calculate the longitude and latitude of point B.

$$J = 1 + \frac{u^2}{16384}\left(4096 + u^2\left[-768 + u^2\left(320 - 175u^2\right)\right]\right) \tag{10}$$

$$K = \frac{u^2}{1024}\left(256 + u^2\left[-128 + u^2\left(74 - 47u^2\right)\right]\right) \tag{11}$$

The latitude of point B can be determined from

$$\tan\phi_B = \frac{\sin U_1\cos\sigma + \cos U_1\sin\sigma\cos\alpha_1}{(1-f)\sqrt{\sin^2\alpha + \left(\sin U_1\sin\sigma - \cos U_1\cos\sigma\cos\alpha_1\right)^2}} \tag{12}$$

The longitude difference P on the auxiliary sphere is computed from

$$P = \arctan2\left(\sin\sigma\sin\alpha_1, \cos U_1\cos\sigma - \sin U_1\sin\sigma\cos\alpha_1\right) \tag{13}$$

Vincenty's constant C (Deakin and Hunter, 2009) can then be computed from

$$C = \frac{f}{16}\cos^2\alpha\left[4 + f\left(4 - 3\cos^2\alpha\right)\right] \tag{14}$$

And the longitude difference on an ellipsoid is then computed from

$$\lambda = P - (1-C)f\sin\alpha\left\{\sigma + C\sin\sigma\left(\cos[2\sigma_m] + C\cos\sigma\left[-1 + 2\cos^2(2\sigma_m)\right]\right)\right\} \tag{15}$$

The longitude of point B can be computed from

$$\lambda_B = \lambda + \lambda_A \tag{16}$$

Table 1. Lag compensation algorithm.

Input: $A(\phi_A, \lambda_A)$, current position of the UAV.
    α_{AB}, azimuth angle.
    a, length of semi-major axis of the ellipsoid.
    b, length of semi-minor axis of the ellipsoid.
    S, compensation distance

Output: Pv, spray volume (L ha^{-1})
    1: Convert the longitude, latitude and azimuth Angle of point A to radian.
    2: Calculate the reduced latitude of point A.
    3: Calculate the angular separation between point A and the equator.
    4: Calculate the forward azimuth of the geodesic at the equator.
    5: Calculate the angular separation between points (first-order).
    6: $\sigma' \leftarrow 0$; iterations $\leftarrow$ 0/*Setting the initial value; iterations= the number of iterations*/
       /*Through multiple iterations, the angular separation σ can be accurately calculated*/
    7: while $(\sigma - \sigma) > 10^{-12}$ do
    8: Get the angular distance on sphere from equator to line midpoint
    9: Calculate Δ_σ
    10: $\sigma' \leftarrow \sigma$
    11: Correct the value of the angular separation σ.
    12: Iterations++
    13: If iterations>100 then /* Iterate 100 times without convergence, return $A(\phi_A, \lambda_A)$*/
    14: Return $A(\phi_A, \lambda_A)$
    15: Break
    16: End while
    17: Get the latitude of point B/* $B(\phi_B, \lambda_B)$, Compensation coordinates */
    18: Calculate the difference in longitude between two points on the auxiliary sphere.
    19: Calculate the difference in longitude between two points on the ellipsoid.
    20: Get the longitude of point B
    21: Convert the longitude, latitude of point B to degree.
    22: Use $B(\phi_B, \lambda_B)$ to obtain the spray volume P_v from the prescription map
    23: Return P_v

For straight lines of any length with a longitudinal difference less than 180 degrees, Vincenty's formulae is capable of determining coordinates to an accuracy on the level of millimeters (Nowak and Nowak Da Costa, 2022). The spray volume (L ha^{-1}) can be obtained from the prescription map according to the compensation coordinates $B(\phi_B, \lambda_B)$.

Pulse width modulation system performance

Performance evaluation methods for pulse width modulation system

When PWM solenoid valves are used to modulate nozzle flowrates, it is highly likely that different designs of PWM solenoid valves will have different response times and flowrates at a specific duty cycle. These variations may have a direct effect on spray characteristics which in turn can affect the quality of foliar coverage and deposition. It is, therefore, necessary to evaluate the performance of PWM-controlled nozzles operating with different numbers of nozzles and DC.

The experiments were conducted in the atomization laboratory of the National Center for International Collaboration Research on Precision Agriculture Aviation Pesticides Spraying Technology with an average environmental temperature of 26°C and an average relative humidity of 40%. The measurement devices are divided mainly into pressure detection devices and flowrate detection devices. The pressure measurement equipment includes a data acquisition card (Yawei Electronic Technology Co., Ltd, Wuhan, China), a pressure transducer (PSE560-01-28, SMC Corporation, Tokyo, Japan), and a laptop computer (Y7000P, Lenovo, Beijing, China). Pressure transducer with measurement capability up to 1MPa and repeatability within 0.2%. The data acquisition card uses 3 acquisition channels to detect the output current value (4~20mA) of the pressure transducer at 1kHz and transmits the digital data to the computer via USB. The current value is then converted to a pressure value using the regression equation for the sensor calibration curve provided by the manufacturer. Finally, the pressure curve is plotted by the LabVIEW-based data acquisition platform. In addition, the flowrates for each treatment combination were measured simultaneously with a flow meter (939-1525/F01, Zhongketeda Technology Co., Ltd, Beijing, China) and beakers. The flow meter has a measurement accuracy of ±3% and a linear

response time of 1ms. The total flowrates were divided by the number of nozzles to determine the flowrates of each nozzle.

The post-valve pressure that acted directly on the nozzle orifice (downstream pressure) and the flowrate were tested. Measurements of these parameters were made for two numbers of nozzles (8 nozzles and 12 nozzles respectively) and for nine duty cycles (from 20% to 100% with an interval of 10%). Each measurement was repeated three times. During the experiment, the data acquisition device continuously recorded pressure data for 3 seconds, providing 3,000 data points for data analysis. The pressure data were used to evaluate the effect of the number of nozzles and duty cycles on the pressure drop and response time of the solenoid valve. The operating pressure is measured with the solenoid valve open and at a steady state between peak and fall times. For comparison, the flowrates for a specific duty cycle and number of nozzles were also calculated. For example, if the measured flowrate at 100% DC and 12 nozzles was 0.5L min^{-1}, the calculated flowrate at 60% DC and the same number of nozzles would be 0.3L min^{-1} according to the following equation:

$$Q_c = Q_{100} \times DC \tag{17}$$

where Q_c is the calculated flowrate (L min^{-1}), Q_{100} the measured flowrate at 100% DC (L min^{-1}), and DC is the corresponding duty cycle (%).

Pressure drop

Figure 5 shows the transient downstream pressure of the PWM system at 12 nozzles and 50% duty cycle. The sum of the peak and fall times within each cycle is 20ms. The actual percentage of time operating at steady pressure is approximately the same as the specified duty cycle. PWM solenoid valves have an on/off time delay before reaching the target application pressure for each cycle. In addition, the controller needs a response time to send a command to turn the solenoid valve on from the off state. The spray system will continue to spray for 10ms after the PWM solenoid valve is powered off. Figure 6 shows the instantaneous downstream pressure of the PWM system at different duty cycles. In the duty cycle range of 50% to 90%, the downstream pressure reaches zero when the valve is closed and increases sharply to the operating pressure when the
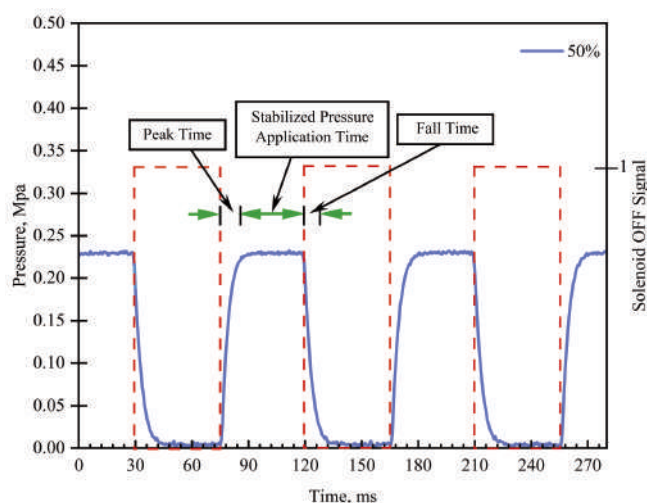
Figure 5. Pressure response of pulse width modulation system with different 12 nozzles at 50% duty cycle.
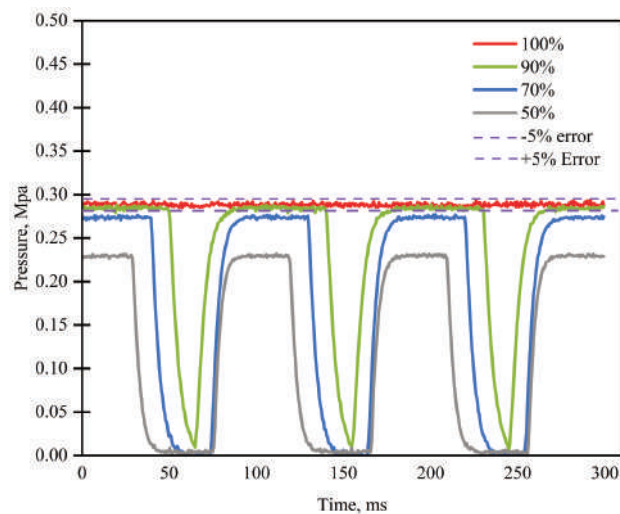
Figure 6. Pressure response of pulse width modulation system with different duty cycle (50%, 70%, 90%, 100%) at 12 nozzles.

valve is open. It is clear that the time to stabilize the downstream pressure decreases as the duty cycle decreases, because the lower the duty cycle, the longer the nozzle stays closed. However, when the duty cycle exceeds 90%, PWM solenoid valves will be in a normally open state because it is less than the minimum response time of the solenoid valve. The steady pressure at a duty cycle of 100% is 290 kPa. As the duty cycle decreases, the steady pressure gradually decreases and is reduced to 227 kPa at a duty cycle of 50%. The maximum pressure drop caused by the pulse width modulated solenoid valve is 21.7%. As indicated by Bernoulli's principle, the fluid structure and the inherent characteristics of the PWM solenoid valve can lead to energy loss. This energy loss can lead to pressure loss. Considering that the operating pressure of PWM-controlled nozzles is usually in the range of 200 to 400 kPa, the operating pressure at 50% duty cycle still meets the requirement (Butts *et al.*, 2019). However, if the duty cycle is further reduced, there may be a risk of changing the spray characteristics.

Flowrates

Table 2 shows the calculated and measured flowrates for the PWM system at different duty cycles. As expected, the average flowrate continues to increase as the duty cycle increases from 20% to 100%. Table 2 shows that the minimum flowrate at 12 nozzles is 0.123L min^{-1} and the maximum spray flowrate at 8 nozzles is 0.534L min^{-1}. The average measured flowrate for both 8 and 12 nozzles is greater than the calculated flowrate. As the number of nozzles decreases, the difference between the calculated and measured flowrates decreases slightly. In addition, there is a slight change in flowrate between 90% and 100% duty cycle, an observation that indicates that the solenoid valve is fully open or closed for no less than 10ms when the valve is operated at high frequency. In most treatments, the flowrate increases linearly with duty cycle

when the duty cycle is between 50% and 90%. But a duty cycle below 50% may result in pressure drop, which can affect the quality of leaf coverage and deposition. Therefore, the duty cycle range was set at 50% to 90%. With the number of nozzles at 8 and 12 respectively, the average flowrate increment for each 10% increase in duty cycle was 0.05L min^{-1} and 0.053L min^{-1}. We can tentatively determine that the flowrate shows a linear variation with duty cycle, but in practice, the flowrate needs to be fitted linearly before the PWM system can be integrated into a variable application. Based on the fitted equation (Eq. 2), duty cycle can be assigned to the VRS system to precisely discharge the spray volume.

Field experiment design

Prescription map design and interpretation

The experimental location is in Anyang, Henan Province, China (114.543487E, 35.996089N). The prescription map contains 40 sub-test areas. The total test area is 2,880 m^2 (120×24m). Each sub-test area is 6m wide and 12m long. The flight height of the UAV was set to 3.5m during the experiment. After path planning, the UAV passed continuously through the center of each sub-test area and sprayed at different spray rates (L ha^{-1}). In this study, the prescription map was artificially designed to test the performance of the VRS system. The prescription map is composed of multiple polygons (sub-test area) containing different spray volumes. First, polygon objects are generated using pre-measured geographic coordinates. Then, spray volumes are added to the polygons. Finally, the geo-coordinate system is imported into the prescription map. The prescription map in vector format (.shp) contains information such as index, polygon coordinates, spray volume and geographic coordinate system. This information is stored in a string format in the attribute table, which is shown in Table 3. When the VRS control

Table 2. Measured and calculated flowrates of pulse width modulation valves at duty cycle ranging from 20% to 100% and number of nozzles (8 Nozzle, 12 nozzles).

Number of nozzles	Type	\multicolumn			Mean flowrate (L min^{-1}) DC (%)			
		100	90	80	70	50	40	20
8	Measured	0.534	0.521	0.435	0.393	0.277	0.234	0.128
8	Calculated	0.530	0.480	0.420	0.370	0.260	0.210	0.110
8	Difference	0.004	0.041	0.015	0.023	0.017	0.024	0.018
12	Measured	0.508	0.496	0.421	0.385	0.273	0.252	0.123
12	Calculated	0.500	0.450	0.400	0.350	0.250	0.200	0.100
12	Difference	0.008	0.046	0.021	0.035	0.023	0.032	0.023

Standard deviations of all mean flowrates were not greater than 0.05 L min^{-1}. DC, duty cycle.

Table 3. Attribute table.

Index	Spray volume (L ha^{-1})	Geometry
0	23.8	POLYGON ((114.54348 35.99608, 114.54360 35.996…))
1	20.5	POLYGON ((114.54352 35.99626, 114.54364 35.996…))
2	16.6	POLYGON (114.54356 35.99644, 114.54369 35.996…))
…		
…		
…		
…	…	
…		
38	17.7	POLYGON ((114.54360 35.99606, 114.54372 35.996…))
39	25.5	POLYGON ((114.54364 35.99623, 114.54377 35.996...))

system is initialized, the prescription map is automatically imported. First, the experiment of the VRS system without LCA was used as a blank experiment. Next, the spray effect of the VRS control system using LCA was tested and compared with a blank experiment. For the two types of experiments mentioned above, the spray volumes were measured at three flight speeds (4, 5, 6m s^{-1}) to evaluate the spray accuracy at different speeds. Each combination was repeated three times and a total of 18 flight tests were performed. During the flight of the UAV, the controller needs to interpret the prescription map in real time. The basic idea of interpreting the prescription map is to determine the polygon to which the compensation coordinates belong and extract the spray volume (L ha^{-1}) from the interior of the polygon. The algorithm for prescription map interpretation is shown in Table 4. We first use the *Point()* function to generate a *point* object based on the compensation coordinates calculated by the lag compensation algorithm. We then loop through to determine the polygon where the point is located, and exit the loop when the polygon is found. Finally, we obtain the spray volume for the polygons that contain the compensated coordinate point (*FlowSearch()*). When all polygons do not contain the point, it indicates that the UAV does not enter within the prescription map and the spray volume defaults to 0L min^{-1}.

Evaluation methods of control system

During operation, GPS coordinates, prescription rates, and actual spray rates are saved in real-time in the controller text file. After that, the information is imported into the ArcGIS (ESRI, USA) software, and the coordinate points are mapped to the prescription map in the software to evaluate the control accuracy and control stability of the system.

The performance of the control system is evaluated according to indicators such as LD and control accuracy. The LD is defined as the distance the VRS system advances before reaching the required spray rate for the new test area. The spray accuracy (*SA*) was used to evaluate the control accuracy of the spray system. The *SA* of the k-th data point (*SA*$_k$) characterizes the difference between the actual spray rate (*S'*$_k$) and the prescription rate (*S*$_k$) at the kth data point in the VRS prescription map, as calculated by Equation (18). After the analysis of *SA,* it is possible to find the latitude and longitude coordinates in the new test area when a stable spray rate is formed. The distance (LD) between the boundary coordinates of the new experimental area and the coordinates when a new stable rate is formed can be obtained through the measurement tool in ArcGIS software. The overall *SA* (%) is then determined using

Equation (Eq. 19):

$$SA_k = (1 - \frac{|S'_k - S_k|}{S_k}) \cdot 100\% \quad (18)$$

$$SA = \frac{1}{N} \cdot \sum_{k=1}^{N} SA_k \quad (19)$$

Evaluation of spray deposition and coverage

Water sensitive paper (WSP; Spraying Systems Inc., Wheaton, IL, USA) is arranged in the test area to capture droplets. The droplet coverage of the VRS system at different spray rates was evaluated by analyzing the number and size of droplets. Three WSP sampling points were arranged in each sub-test area, and a schematic diagram of the sampling points is shown in Figure 7. Along each steel tube planted in the ground, two pieces of WSP were held with double-ended clamps at distances of 0.5m and 1m from the ground. The steel tubes are lined up in 3 rows along the direction of UAV flight, with each row spaced 2 meters apart according to the width of the UAV spray. There were two columns of sampling points spaced 2 m apart in each sub-test area. A weather station (NL-5G, Zhejiang Top Cloud-agri Technology Co., Ltd. China) was used to monitor the environmental conditions throughout the experiment. The weather station was equipped with an acoustic anemometer to measure wind speed and direction relative to the spray track, and two temperature hygrometers to measure air temperature and relative humidity. The average air temperature was 27.5°C, the average relative humidity was 45.5%, and the average wind speed recorded for each test was always below 1.35 m s^{-1}. After each test, the WSPs were allowed to dry before being collected in labeled self-sealing bags and then placed in a dry cooler so that the cards could be safely transferred to the lab. Spray deposition images of each WSP were acquired using a Hewlett-Packard scanner at 600-dpi imaging resolution. Next, spray coverage and deposition density on each WSP were analyzed from these images using the WSP sample deposition analysis software (DepositScan) (Zhu *et al.*, 2011). In the analysis process, spray coverage and deposition density were used to evaluate the spray effect. Spray coverage (%) was calculated as the percentage area covered with the spray deposits on the WSP and deposits density (deposits cm^{-2}) was determined as the number of spray deposit stains per unit of WSP target area (Cerruto *et al.*, 2019).

Table 4. Interpretation of prescription map.

Input: P*oint*, the point object of the current coordinate or compensation coordinate
       G$_i$, the polygon objects in the prescription map
       L$_{num}$, the number of polygons

Output: *P*$_v$, the spray volume
    1: P*oint* ← *Point(φ, λ)*/* Generate point object */
    2: N ← 1
    3: For each *i* ∈ *G*$_i$ do/* Generate point objects */
    4: If *i* contains(*point*) then/* Determine if the point object is a polygon */
    5: *P*$_v$ ← *FlowSearch(N-1)*/* Get spray volume */
    6: Break
    7: Else:
    8: N ← N+1
    9: If (N=*L*$_{num}$) then
    10: *P*$_v$ ← 0
    11: Return *P*

Results and Discussion

Lag distance and spray accuracy

Figure 8a shows the LD for different spray rates at a flight speed of 5 m s^{-1}. The results showed that the range of LD of the VRS system with LCA was -0.27~0.78m, with an average LD of 0.32m, while the LD of the VRS system without LCA was 3.5~4.3m, with an average LD of 3.87m. The experiments demonstrated that the LCA developed in this work was significantly effective in reducing the LD values. The LD values of the VRS system with LCA were significantly lower than those of the system without LCA, with an average LD value reduction of 3.55m. There was no significant pattern in the change of LD values as the spray rate

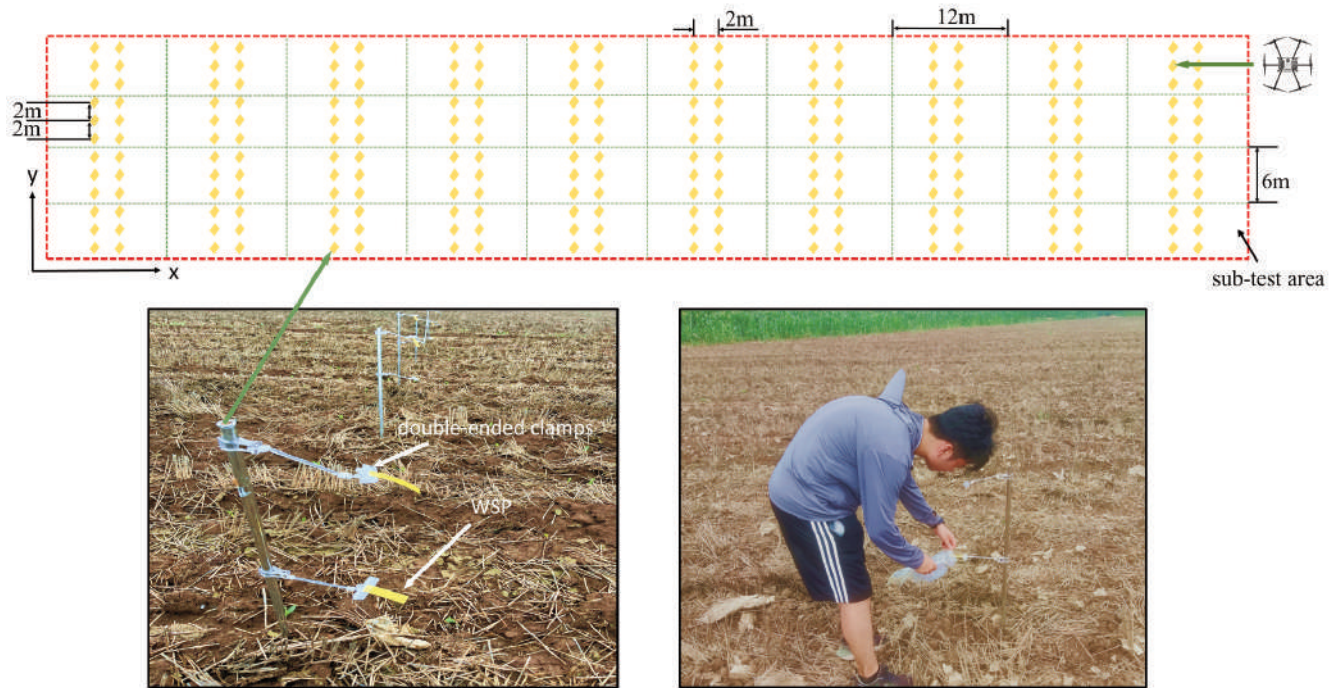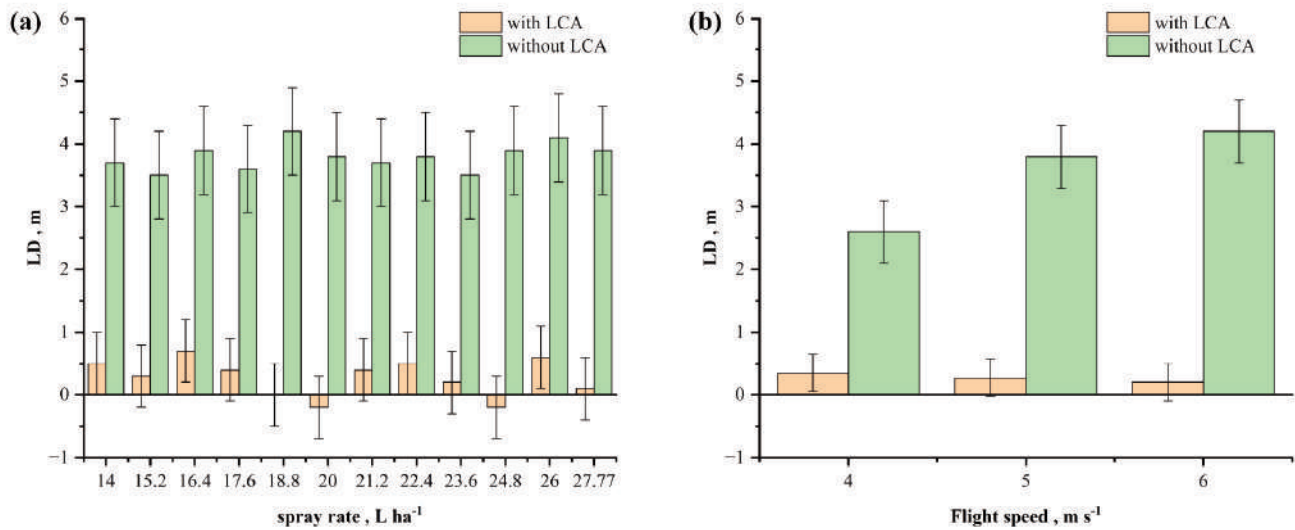**Figure 7.** Schematic diagram of sampling points.

Figure 8. (**a**) Lag distance values at different spray rates (with lag compensation algorithm and without lag compensation algorithm), (**b**) lag distance values at different flight speeds (with lag compensation algorithm and without lag compensation algorithm).

increased or decreased, indicating that the change in spraying rate of the VRS system did not have a significant effect on LD values (P>0.05). Similarly, based on the LD, it can be seen that the PWM system maintains a fast response time when changing the spraying rate. Figure 8b shows the results of LD obtained from contrast trials conducted under different flight speeds with and without LCA. The system without LCA shows a strong correlation between LD and flight speed, with faster flight speed corresponding to larger LD values. For a flight speed of 6m/s, the average LD value is 4.2m s^{-1}. However, the LD values of the VRS system with LCA did not change significantly with the change in flight speed. The VRS system with LCA can automatically adjust the compensation distance S according to the flight speed, which effectively reduces the effect of flight speed on the LD values. Therefore, the VRS system can maintain a low LD value at different speeds. Table 5 summa-

rizes the spray accuracy (SA) of the VRS system obtained at different flight speeds and spray rates. During the spraying process, the SA values ranged from 91.56% to 97.32%, with an average value of 94.77%. As the flight speed increases, the SA value increases slightly, which indicates that the control system obtains higher control accuracy as the flight speed increases. The increase in spray accuracy may be related to the control accuracy of the flowmeter. The increase in flight speed caused an increase in the spray rate (L min^{-1}), and the measurement accuracy of the flowmeter increased with the increase in the spray rate.

Deposition density and coverage

Figure 9 shows the results of spray coverage (SC) obtained under real field conditions at different heights through a color map
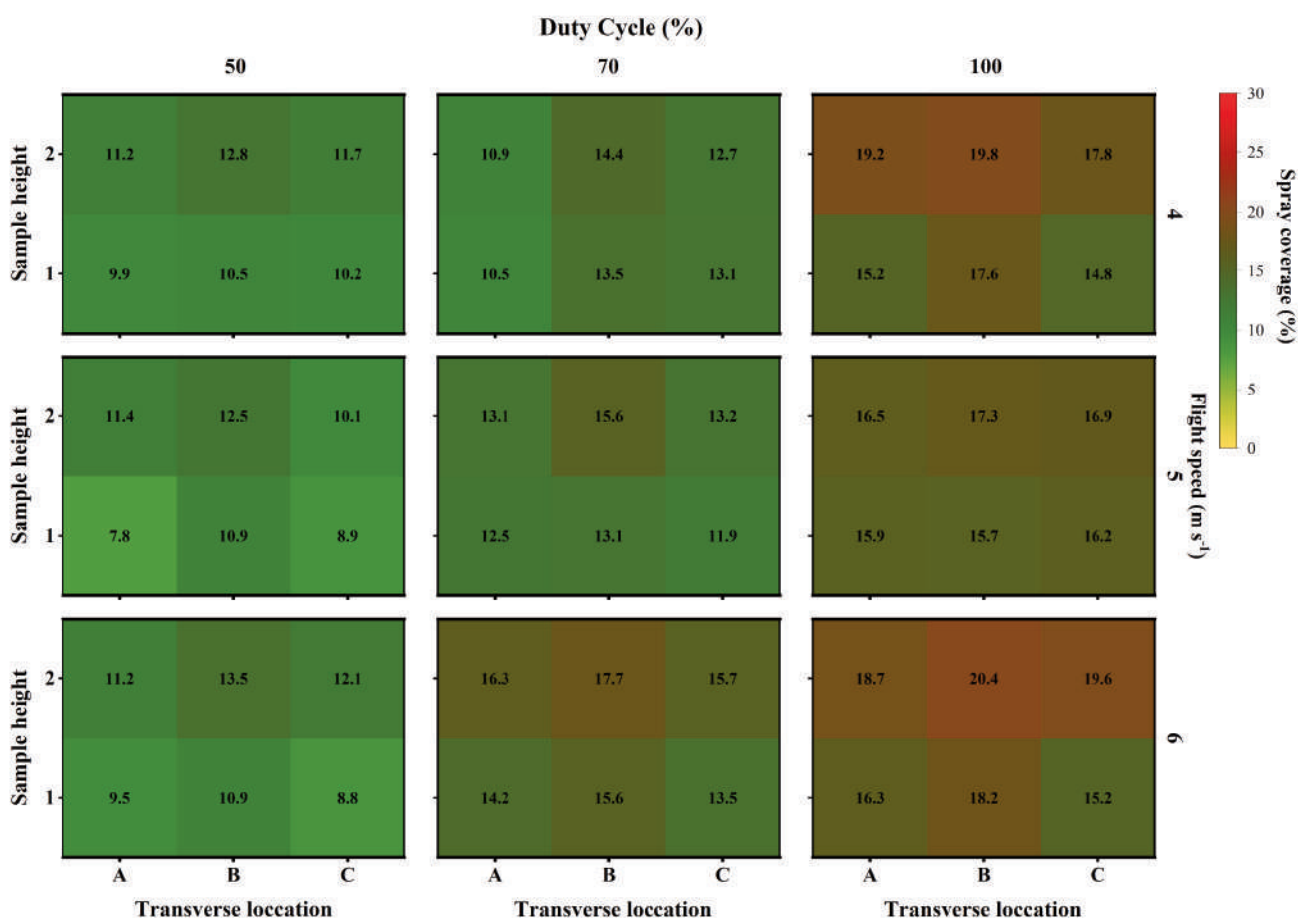
Figure 9. Mean spray coverage on the water sensitive paper at different heights (1=0.5m, 2=1.0m) and transverse locations (A=right edge; B=middle; C=left edge) for the different flight speed and duty cycle combinations.

Table 5. The spray accuracy (SA) of the variable-rate spray system obtained at different flight speeds and spray volumes.

| Flight speed (m s^{-1})	Spray volume (L ha^{-1})									
	14.5	15.4	16.6	17.7	19.4	20.5	22.7	23.8	25.5	27.8
4	91.56	92.63	93.26	93.55	94.62	94.34	95.28	95.33	95.88	96.48
5	93.73	93.28	93.43	94.58	95.46	94.69	94.74	95.67	96.27	96.09
6	93.66	93.84	94.23	94.66	95.85	95.16	95.81	95.61	96.31	97.32

for different flight speed and duty cycle combinations. As expected, the higher the spray rate for a given flight speed the higher the spray coverage can be obtained. In addition, the spray coverage of the upper layer was consistently higher than the spray coverage of the lower layer. It can be seen that the height of the sampling point significantly affects the spray coverage. SC also shows a slight difference in transverse location. Transverse non-uniformity is more pronounced at 50% duty cycle, with an average difference of 1.62% in SC between the center and sides, further indicating that low duty cycle affects spray width and overall area coverage. In addition, the effects of flight speed and duty cycle on spray coverage can be attributable to differences in the spray volume, and no significant interaction effects were found for SC.

Figure 10 shows the spray coverage and deposition density at different flight speeds and sub-test areas. The spray coverage ranged from 7.8% to 20.4% when the flight speed was 5m s^{-1}, with an average coverage of 14.3%. It is important to note that a higher spray coverage does not necessarily mean a more effective spraying. In other words, spray coverage can be reduced appropriately without affecting the effectiveness of the chemical composition (Zhu *et al.*, 2011). Spray coverage of more than 30% was classified as overspray according to Chen *et al.* (2013). From the spray coverage in Figure 10, it can be seen that the VRS system did not overspray. As the flight speed increased, the average spray coverage increased from 13.4% at 4m s^{-1} to 14.9% at 6m s^{-1}. The increase in spray coverage was caused by the down-pressure wind field of the

UAV that made it easier for water droplets to be deposited on the WSP. However, when the duty cycle is 50% to 60%, the wind field causes more droplet drift, which deflects the droplets off target. Therefore, the wind field makes better droplet deposition when a high-duty cycle is used, while it makes worse droplet drift when a low-duty cycle is used.

The quality of droplet distribution is related to the deposition density of the target surface. For example, deposition densities of 20~40 (deposits cm^{-2}) are recommended for insecticides to achieve effective pest control (Miranda *et al.*, 2021). Deposition densities of 30 and 70 (deposits cm^{-2}) were used as reference values for effective insecticides and fungicides, respectively. Fungicides require higher deposition densities, so higher flight speeds are not recommended to prevent drift of droplets. As shown in Figure 10, the deposition density varies from 15.2 to 75.3 (deposits cm^{-2}). Sample points with deposition densities between 30 and 70 (deposits cm^{-2}) accounted for 77.5% of the total samples when the flight speed was 4 m s^{-1}. Sample points with deposition densities between 30 and 70 (deposits cm^{-2}) accounted for 87.5% of the total samples when the flight speed was 6 m s^{-1}. The average deposition density in all collected samples was 46.5 (deposits cm^{-2}). In addition, the deposition density of the sample does not always increase with increasing spray volume, due to the fact that multiple droplets may combine together which can lead to software calculation errors. While coverage and deposition density are useful variables to study the efficiency of spray systems, future biological efficacy
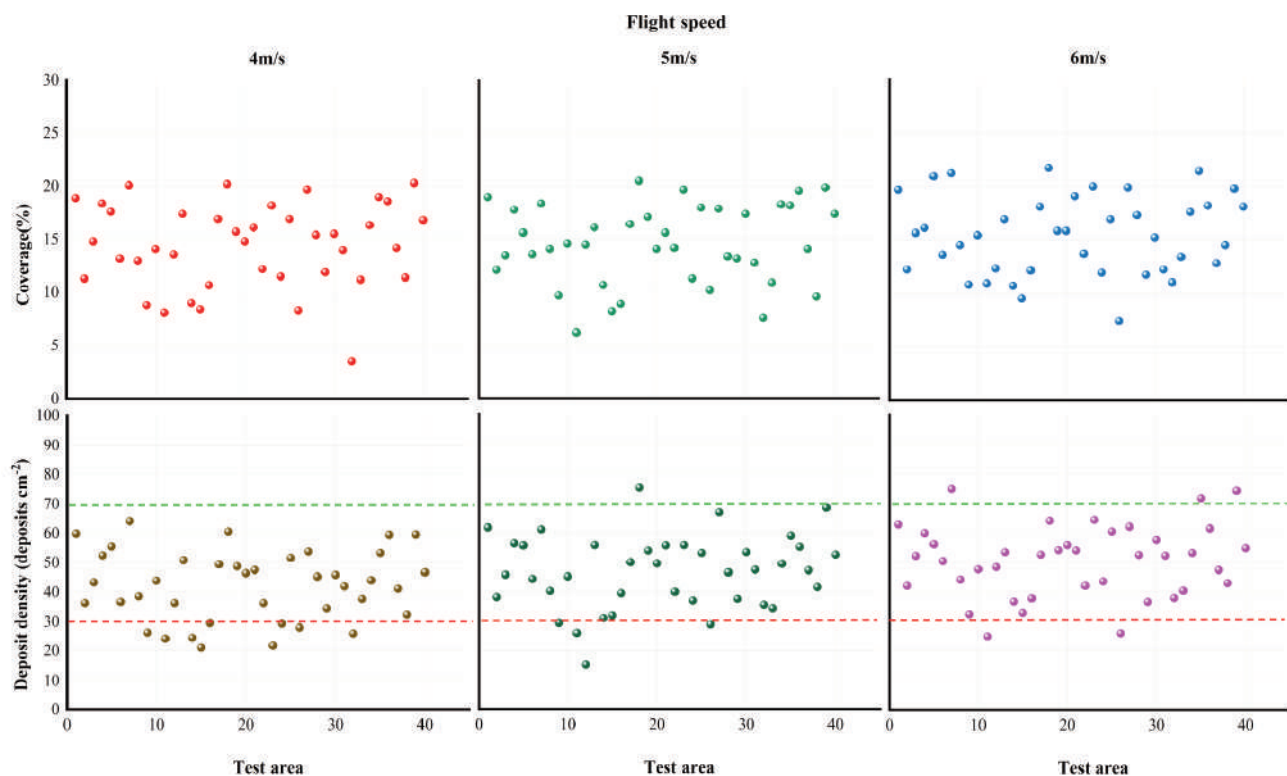
Figure 10. Plots of deposit density (deposits cm^{-2}) and spray coverage (%) for the different flight speed and spray rate combinations. Horizontal red and green dashed lines represent the deposition density reference values for effective insecticide (30 deposits cm^{-2}) and fungicide applications (70 deposits cm^{-2}), respectively.

tests are needed to understand the true biological effects of each spray rate.

Conclusions

The UAV-based VRS system is an effective means of applying variable spraying for precision agriculture. The system is able to apply pesticides quickly to crops at different spray rates, avoiding excessive spray deposition while largely ensuring the effectiveness of the pesticides. In particular, the following conclusions may be drawn from the experimental results:

(1) The PWM system can reduce the flowrates while maintaining a reasonable operating pressure. The duty cycle varies linearly with the flowrate and the difference between the calculated and measured flowrates is less than 0.05 L min^{-1}. As the duty cycle is reduced from 100% to 50%, the pressure drop does not exceed 63 kPa. Therefore, the flowrate of the PWM system can be precisely adjusted according to the duty cycle.

(2) Field trial tests showed that the lag compensation algorithm has effectively reduced the spraying LD, which in turn improved the spraying accuracy of the VRS system. The optimized VRS system can achieve 94.77% average spraying position accuracy. The spraying accuracy of VRS system increases with the increase in flight speed.

(3) The results of deposition density and spray coverage measured with WSP showed that there were differences in droplet deposition at different heights and transverse locations. The overall spray coverage ranged from 7.8% to 20.4%, with no overspray. The average spray coverage increased gradually with increasing flight speed, with the highest average spray coverage being 14.9%. When the flight speed was 6 m s^{-1}, the sampling points with deposition densities ranging from 30 (deposits cm^{-2}) to 70 (deposits cm^{-2}) accounted for 87.5% of the total samples, and the average deposition density was 46.5 (deposits cm^{-2}).

Overall, the VRS system can perform variable rate spraying tasks at site-specific based on prescription maps and has acceptable quality in terms of coverage, deposition density, and droplet diameter. Thus, the system improves production efficiency and reduces environmental pollution by reducing the use of pesticide chemicals. However, the impact of pesticide reduction on biological efficacy is unclear and more detailed field trials are needed depending on the specific crop.

References

Baio F.H.R., Neves D.C., Souza H.B., Leal A.J.F., Leite R.C., Molin J.P., Silva S.P. 2018. Variable rate spraying application on cotton using an electronic flow controller. Precis. Agric. 19:912-28.

Biglia A., Grella M., Bloise N., Comba L., Mozzanini E., Sopegno A., Pittarello M., Dicembrini E., Alcatrão L.E., Guglieri G. 2022. Uav-spray application in vineyards: flight modes and spray system adjustment effects on canopy deposit, coverage, and off-target losses. Sci. Total Environ. 845:157292.

Butts T.R., Butts L.E., Luck J.D., Fritz B.K., Hoffmann W.C., Kruger G.R., 2019. Droplet size and nozzle tip pressure from a pulse-width modulation sprayer. Biosyst. Eng. 178:52-69.

Cerruto E., Manetto G., Longo D., Failla S., Papa R. 2019. A model to estimate the spray deposit by simulated water sensitive papers. Crop Prot. 124:104861.

Chen P., Ouyang F., Wang G., Qi H., Xu W., Yang W., Zhang Y., Lan Y. 2021. Droplet distributions in cotton harvest aid applications vary with the interactions among the unmanned aerial vehicle spraying parameters. Ind. Crop. Prod. 163:113324.

Chen Y., Ozkan H.E., Zhu H., Derksen R.C., Krause C.R. 2013. Spray deposition inside tree canopies from a newly developed variable-rate air-assisted sprayer. T. Asabe. 56:1263-72.

Deakin R.E., Hunter M.N. 2009. Geodesics on an ellipsoid-bessels method. School of Mathematical and Geospatial Sciences, RMIT University.

Fabiani S., Vanino S., Napoli R., Zajíček A., Duffková R., Evangelou E., Nino P. 2020. Assessment of the economic and environmental sustainability of variable rate technology (vrt) application in different wheat intensive european agricultural areas. A water energy food nexus approach. Environ. Sci. Policy. 114:366-76.

Giles D.K., Comino J.A. 1989. Variable flow control for pressure atomization nozzles. SAE transactions. pp. 237-49.

Gómez-Candón D., De Castro A.I., López-Granados F. 2014. Assessing the accuracy of mosaics from unmanned aerial vehicle (uav) imagery for precision agriculture purposes in wheat. Precis. Agric. 15:44-56.

Gómez-Candón D., López-Granados F., Caballero-Novella J.J., Peña-Barragán J.M., García-Torres L. 2012. Understanding the errors in input prescription maps based on high spatial resolution remote sensing images. Precis. Agric. 13:581-93.

Grella M., Gioelli F., Marucco P., Zwertvaegher I., Mozzanini E., Mylonas N., Nuyttens D., Balsari P. 2022. Field assessment of a pulse width modulation (pwm) spray system applying different spray volumes: duty cycle and forward speed effects on vines spray coverage. Precis. Agric. 23:219-52.

Huang Y., Hoffmann W.C., Lan Y. 2008. Development of an unmanned aerial vehicle-based spray system for highly accurate site-specific application. In: 2008 Providence, Rhode Island, June 29-July 2, 2008. Am. Soc. Agric. Biol. Eng. p. 1.

Hunter J.E., Gannon T.W., Richardson R.J., Yelverton F.H., Leon R.G. 2020. Integration of remote weed mapping and an autonomous spraying unmanned aerial vehicle for site specific weed management. Pest Manag. Sci. 76:1386-92.

Jay M.L. 2003. Trends in agricultural aviation: bright spots ahead. Agric. Aviation. 30:18-23.

Jensen H.G., Jacobsen L., Pedersen S.M., Tavella E. 2012. Socioeconomic impact of widespread adoption of precision farming and controlled traffic systems in denmark. Precis. Agric. 13:661-77.

Koo Y. 2019. Nozzle pressure response characteristics of variable rate system for unmanned aerial applications. J. Biosyst. Eng. 44:1-11.

Mancini A., Frontoni E., Zingaretti P. 2019. Challenges of multi/hyper spectral images in precision agriculture applications. IOP conference series. Earth Environ. Sci. 275:12001.

Mangus D.L., Sharda A., Engelhardt A., Flippo D., Strasser R., Luck J.D., Griffin T., 2017. Analyzing the nozzle spray fan pattern of an agricultural sprayer using pulse width modulation technology to generate an on-ground coverage map. T. Asabe. 60:315-25.

Miranda M.P., Da Silva Scapin M., Vizoni M.C., Zanardi O.Z., Eduardo W.I., Volpe H.X.L. 2021. Spray volumes and frequencies of insecticide applications for suppressing diaphorina citri populations in orchards. Crop Prot. 140:105406.

Nowak E., Nowak Da Costa J. 2022. Theory, strict formula derivation and algorithm development for the computation of a geodesic polygon area. J. Geodesy. 96:1-23.

Qi H., Zhou J., Li C., Chen P., Liang Y., Huang G., Zou J. 2021. Feasibility of variable rate spraying of centrifugal uav using network rtk. Trans. Chin. Soc. Agric. Eng. 37:81-9.

Salcedo R., Zhu H., Jeon H., Ozkan E., Wei Z., Gil E. 2022. Characterisation of activation pressure, flowrate and spray angle for hollow-cone nozzles controlled by pulse width modulation. Biosyst. Eng. 218:139-52.

Salcedo R., Zhu H., Ozkan E., Falchieri D., Zhang Z., Wei Z., 2021. Reducing ground and airborne drift losses in young apple orchards with pwm-controlled spray systems. Comput. Electron. Agr. 189:106389.

Salcedo R., Zhu H., Zhang Z., Wei Z., Chen L., Ozkan E., Falchieri D. 2020. Foliar deposition and coverage on young apple trees with pwm-controlled spray systems. Comput. Electron. Agr. 178:105794.

Seong J.C., Choi J. 2007. Geodist: a c++ program for calculating geodesic distances with a shapefile. Comput. Geosci.-Uk. 33:705-8.

Shi Q., Liu D., Mao H., Shen B., Li M. 2021. Wind-induced response of rice under the action of the downwash flow field of a multi-rotor uav. Biosyst. Eng. 203:60-9.

Silva J.E., Zhu H., Cunha J.P.A.R. 2018. Spray outputs from a variable-rate sprayer manipulated with pwm solenoid valves. Appl. Eng. Agric. 34:527-34.

Smith L.A. 2001. Automatic flow control for aerial applications. Appl. Eng. Agric. 17:449.

Thomson S.J., Smith L.A., Hanks J.E. 2009. Evaluation of application accuracy and performance of a hydraulically operated variable-rate aerial application system. T. Asabe. 52:715-22.

Yang C., Martin D.E. 2017. Integration of aerial imaging and variable-rate technology for site-specific aerial herbicide application. T. Asabe. 60:635-44.

Yang S., Yang X., Mo J. 2018. The application of unmanned aircraft systems to plant protection in china. Precis. Agric. 19:278-92.

Zhu H., Lan Y., Wu W., Hoffmann W.C., Huang Y., Xue X., Liang J., Fritz B. 2010. Development of a pwm precision spraying controller for unmanned aerial vehicles. J. Bionic Eng. 7:276-83.

Zhu H., Salyani M., Fox R.D. 2011. A portable scanning system for evaluation of spray deposit distribution. Comput. Electron. Agr. 76:38-43.